PHYSICAL REVIEW E **68**, 061405 (2003)

Phase diagram of a quasi-two-dimensional colloid assembly

Derek Frydel and Stuart A. Rice
Department of Chemistry and The James Franck Institute, The University of Chicago, Chicago, Illinois 60637, USA

(Received 9 July 2003; published 18 December 2003)

We report the results of simulations of the phase diagrams of a quasi-two-dimensional (Q2D) colloid assembly and of a two-dimensional (2D) colloid assembly which have the same colloid-colloid interaction. That interaction is the same as used in the study reported by Zangi and Rice [Phys. Rev. E **58**, 7529 (1998)]. Among the goals of the work reported are elucidation of the influence of small amplitude out-of-plane motion on the phase diagram of a system and determination of the effect of that motion on the role of a hexatic phase in the melting process. Both of the systems we have studied undergo a first-order solid I–solid II and solid II–solid III isostructural transition induced by the attractive and repulsive components of the interaction, respectively. Introduction of the out-of-plane motion shifts the low density portion of the phase boundaries involving the solid II phase. The liquid–solid I coexistence line is nearly the same for the two systems. The solid II–solid III transition is shifted to lower temperature and shifted to higher density in the quasi-two-dimensional system. We further use the simulations to calculate the elastic constants, which can be used to predict the location of the Kosterlitz-Thouless-Halperin-Nelson-Young (KTHNY) melting transition. For the Q2D system we find that the first-order melting transition preempts the KTHNY transition for the reduced temperatures $T^* = 1.00$, 0.60, and 0.50. For the 2D system, when $T^* = 0.60$, the KTHNY transition barely preempts the first-order melting transition and when $T^* = 1.00$ and 0.50 the ordinary first-order transition preempts the KTHNY transition.

DOI: 10.1103/PhysRevE.68.061405 PACS number(s): 82.70.Dd, 64.70.Dv

I. INTRODUCTION

It has been known for some time that the nature and degree of spatial ordering that a molecular system supports depend on the dimensionality of the space to which it is confined [1,2]. For example, in one- and two-dimensional systems fluctuations can destroy long-range order of certain types. Consequently, the character of the phase transitions and the phase boundaries for one-, two-, and three-dimensional systems composed of the same molecular species is different despite the common molecule-molecule interactions.

Considerable attention has been focused on understanding the phase diagrams of strictly two-dimensional (2D) systems. At present, the Kosterlitz-Thouless-Halperin-Nelson-Young (KTHNY) theory [3–7] is the most widely accepted description of two-dimensional melting. This theory is based on a characterization of the two-dimensional solid as a deformable medium with inclusion of the two classes of point topological defects with smallest excitation energy to mediate structural changes; it relates the melting process to the mechanical instability of the two-dimensional solid. Although the theory allows for other possibilities [8,9], it is commonly taken to predict that a two-dimensional system that supports only one ordered solid phase melts via sequential continuous phase transitions. The first transition is from the solid with quasi-long-range positional order and long-range bond orientation order to a phase with short-range positional order and quasi-long-range bond orientation order, the hexatic phase. This transition is driven by the dissociation of bound dislocation pairs in the solid. The second transition transforms the hexatic phase to the liquid phase in which both positional and bond orientation order have short range; it is driven by dissociation of individual dislocations to form disclinations.

It has been established, from simulation studies, that in a 2D system the number and nature of the stable phases possible and the orders of the transitions between those phases depend on the range of the intermolecular interaction [10]. Of particular interest to us is the case when the pair interaction has an attractive component and/or a soft repulsive component that has a range that is only a few percent of the molecular diameter. Interactions of this type are believed to be appropriate for the description of a class of colloid systems [11,12]. In this case, as shown by Bladon and Frenkel [10], the 2D colloid system supports an isostructural solid I–solid II transition. In the vicinity of the critical temperature for this isostructural transition, fluctuations can induce formation of a hexatic phase. These fluctuations can also influence the character of the phase transitions at lower densities. In fact, a two-dimensional system with an interaction of the type described can exhibit first-order liquid-to-hexatic, hexatic–solid I, and solid I–solid II transitions. Chou and Nelson [13] extended the KTHNY theory to the case when the two-dimensional system supports two ordered solid phases by incorporating an explicit isostructural solid-to-solid transition in their construction of the elastic free energy. Their analysis assumes that the elastic free energy of the system includes a term descriptive of the strain arising from the change in density associated with that transition. With this assumption it is found that the modified KTHNY theory can account for all of the essential results of the simulation studies of Bladon and Frenkel. However, the Chou-Nelson analysis does not provide a microscopic explanation for the existence of the isostructural solid-to-solid phase transition (which it assumes to exist), i.e., it does not provide *a priori* guidance as to when the elastic free energy of a two-dimensional system should or should not contain the extra contribution from the strain arising from the change in den-

1063-651X/2003/68(6)/061405(16)/$20.00

sity associated with an isostructural solid-to-solid transition.

When the interaction between particles is either of shorter or longer range than the type considered by Bladon and Frenkel the melting behavior of the two-dimensional system is different. For a system that contains hard disks the best available evidence from studies of the elastic moduli suggests that the KTHNY continuous transition from the solid to a liquid phase just barely preempts the solid-to-liquid first-order transition. The available experimental data, obtained from studies of a quasi-two-dimensional (Q2D) colloid assemblies, lead to the conclusion that the solid phase undergoes a first-order transition directly to the liquid phase. This conclusion is not, despite appearances, in conflict with the theoretical studies of 2D hard disks for two reasons. First, the resolution of the system density in those experiments was only of order 2%. Second, and more important, we show in Sec. IV that the change from 2D to Q2D confinment alters the character of the solid-to-hexatic transition. For a 2D system in which the range of the attractive interaction between particles is of the order of the particle diameter or greater, there is not isostructural solid-to-solid transition, and the best available evidence suggests that the melting of the ordered phase to the liquid involves two continuous transitions, one from the solid to the hexatic phase and another from the hexatic phase to the liquid.

Much less attention has been focused on understanding the phase diagrams of systems that are quasi-two-dimensional, i.e., those systems in which out-of-plane molecular motion cannot be eliminated. However, it is just this class of systems that best represents experimental realizations of "two-dimensional matter." The issue to be resolved is whether the small amplitude out-of-plane molecular motion generates only small quantitative corrections to the phase diagram predicted under the assumption that the molecular motion is strictly two dimensional, or if it generates qualitative changes to that phase diagram. In an earlier paper [14] we reported the results of extensive simulations of several phase transitions in a quasi-two-dimensional system designed to mimic a real colloid assembly. The colloid-colloid interaction used in those simulations has an attractive component with a range that is only a few percent of the molecular diameter, and a soft repulsive component of comparable range that connects the attractive well and a very steep repulsive interaction. The simulations were restricted to thermodynamic states with reduced temperature $T^*=1$ (see the next section for a definition). The results of the simulations establish the occurrence of first-order liquid-to-hexatic and hexatic-to-solid transitions, in agreement with the experimental results of Marcus and Rice [12]. The results of the simulations also reveal, at higher densities, an isostructural solid-to-solid transition and a buckling transition, both of which are continuous. The dislocation pair, free dislocation, and free disclination concentrations found in the simulations do not satisfy the predictions of the KTHNY theory.

The research described in this paper addresses two questions. First, what is the topology of the full phase diagram for a Q2D colloid system with particle-particle interaction of the type just described? Second, what is the difference in behavior of the elastic moduli of 2D and Q2D colloid assemblies? This paper reports the results of simulations of the model colloid assembly studied by Zangi and Rice [14] for a number of different temperatures, thereby permitting a more complete construction of its phase diagram. We also report the results of simulations of a model colloid assembly that has the same interactions but which is constrained to have strictly two-dimensional motion. A comparison of the phase diagrams of the quasi-two-dimensional and strictly two-dimensional systems reveals the influence of out-of-plane motion on the locations of the phase boundaries and the ability of the system to support particular ordered arrangements of the particles. Overall, the most apparent macroscopic consequence of permitting out-of-plane motion, thereby converting a 2D system to Q2D, is a shift of some of the phase boundaries to higher densities. These shifts are most visible for the low temperature–low density portion of the liquid–solid II transition line, and for the low temperature–low density portion of the solid I–solid II transition line. As expected, introduction of the out-of-plane motion increases the density range in which the liquid is stable. Simply put, at any selected density at which the liquid is stable its entropy is increased by allowing out-of-plane motion. Similarly, allowing out-of-plane fluctuations in the solid I structure increases its entropy and thereby extends the density range over which it is stable. Eventually the density becomes so large that the puckered structure of solid II becomes unstable. The preceding comments describe the 2D and Q2D phase diagrams when $T^*<0.5$. For $T^*>0.5$ the liquid–solid I coexistence region is very nearly the same for the 2D and Q2D systems.

A comparison of the density dependencies of the renormalized elastic moduli of the 2D and Q2D systems reveals the following. For the 2D system, when the reduced temperature $T^*=0.60$, the KTHNY transition barely preempts the first-order melting transition from solid to hexatic, and when $T^*=1.00$ and 0.50 the ordinary thermodynamic first-order transition from the solid to the hexatic phase preempts the KTHNY transition between those phases. On the other hand, for the Q2D system, we find that when $T^*=0.50$, 0.60, and 1.00 the ordinary thermodynamic first-order transition from the solid to the liquid phase preempts the KTHNY transition between those phases. Clearly, the change from 2D to Q2D geometry has an important effect on the character of the phase transition in the system studied.

II. MODEL SYSTEM AND COMPUTATIONAL DETAILS

A. The model system

The model system studied in this paper is the same as that studied by Zangi and Rice [14]. The colloid-colloid interaction used in the simulations has the form (see inset of Fig. 1 below)

$$u(r^*)=-\varepsilon\exp\left[-\left(\frac{r^*-wc^*}{ww^*}\right)^4\right]+2\times10^{-19}\varepsilon\left(r^*-\frac{1}{2}\right)^{-64}+1.2\varepsilon\exp\left[-\left(\frac{r^*-0.96}{0.074}\right)^8\right]. \tag{1}$$

In all that follows we will use the reduced variables T^*

$=k_BT/\varepsilon$ and $\rho^*=\rho\sigma^2$, with $\rho=N/\mathcal{A}$; the corresponding reduced microscopic coordinates are $r^*=r/\sigma$, $z^*=z/\sigma$, $m=1$, with σ the effective "hard-core" diameter, N the number of particles, and $\mathcal{A}$ the area of the simulation cell. The first term in Eq. (1) represents the attraction between brush-stabilized colloid particles when there is incipient overlap between the brushes attached to their surfaces; the depth of this attractive well is ε and its width is $ww/\sigma=ww^*=0.006$, centered at $wc^*=1.05$. The second term in Eq. (1) is the core-core repulsion, which is the dominant contribution to $u(r^*)$ for colloid-colloid separations $r^*\leqslant 1$. The functional form chosen is very nearly a hard-core repulsion but has continuous derivatives. Using Eq. (1), the colloid-colloid interaction energy is 5.0ε when $r^*=1$; for $r^*<1$ the interaction energy increases very rapidly, hence the identification of σ with an effective "hard-core" diameter. The last term in Eq. (1) is an interpolating soft repulsion, representing the entropy cost associated with interpenetration of the stabilizing brushes attached to the surfaces of the colloid particles. We call the form displayed in Eq. (1) the MR potential.

The colloid particles were also subject to a one-body external potential in the z direction, corresponding to their localization in a cell of height $H/\sigma=H^*=1.2$ (see inset of Fig. 3 below):

$$u_{\text{ext}}(z^*)=2\times 10^{24}(z^*)^{24}. \tag{2}$$

We note that z^* is defined to be the distance from the center of the simulation cell to the center of mass of the colloid particle.

The model system studied in this paper is (except for the size) the same as that studied by Zangi and Rice. For many of the calculations it has 504 particles contained in a rectangular box with side lengths in the ratio $x/y=7/(4\times\sqrt{3})$; other situations are described below. The height of the simulation box, H, is fixed at 1.2σ. Periodic boundary conditions were imposed on the simulation cell in the x and y directions, but not in the z direction. The same number of particles was present in the simulation cell for all of the densities studied. To change the system particle density we changed the area of the simulation cell.

We have used simulation cells with different numbers of particles for different purposes. All of the free energy calculations of the properties of the solid and liquid states described below were carried out with 504 colloid particles, whereas the elastic constant calculations and the structure factor calculations were carried out with 2016 particles. If the number of particles associated with a calculation is not explicitly mentioned, the default number is 2016.

The use of only 504-particle simulation samples to calculate the free energies of the liquid and solid phases was dictated by the goal of our investigation, namely, determination of the phase diagram of the system over a range of ρ^* and T^*. In the studies reported in this paper the free energies of the phases were calculated by construction of a reversible path ξ from a reference state (I) with known free energy to the state of interest (II), which requires simulations for many values of ξ (see below). This requirement, coupled with the time needed to simulate a system with 2016 particles, led to the decision to reduce the simulation sample to 504 particles. The disadvantage of this reduction in system size is, of course, the enhancement of finite-size effects.

B. Calculation of the phase diagram

To map the phase diagram of the colloid assembly we applied the common tangent construction to the free energy densities of the two phases at fixed temperature, to obtain the densities of the coexisting phases. As the free energy cannot be measured directly in a simulation, we calculate it by thermodynamic integration along a defined thermodnamic path. Specifically, we construct a reversible path between a reference state with known Helmholtz free energy and the state of interest, and then evaluate

$$A_{\text{II}}=A_{\text{I}}+\int_{\text{I}}^{\text{II}} d\xi\,\frac{\partial A(\xi)}{\partial\xi}. \tag{3}$$

In Eq. (3), ξ is a continuous variable that parametrically connects the reference state I to the state of interest II. For a state in the liquid phase with density ρ and temperature T we choose the ideal gas at the same temperature as the reference state; with this choice $\xi=\rho$. Then

$$A[\rho,T]=A[\rho_{\text{ref}},T]+\int_{\rho_{\text{ref}}}^{\rho} d\rho'\left(\frac{\partial A(\rho')}{\partial\rho'}\right)_T. \tag{4}$$

Note that ρ is defined as $N/\mathcal{A}$ for both 2D and Q2D colloid assemblies. We take ρ_{ref} in Eq. (4) to be the density at which our colloid system and an ideal gas are indistinguishable. Then, at the same temperature and density we can write $A[\rho_{\text{ref}},T]=A_{\text{id}}[\rho_{\text{ref}},T]$; the subscript "id" indicates the ideal gas. The free energy of the liquid is then representable in the form

$$\begin{aligned}A[\rho,T]&=A_{\text{id}}[\rho_{\text{ref}},T]+\int_{\rho_{\text{ref}}}^{\rho} d\rho'\left(\frac{\partial A(\rho')}{\partial\rho'}\right)_T\\&=A_{\text{id}}[\rho,T]-(A_{\text{id}}[\rho,T]-A_{\text{id}}[\rho_{\text{ref}},T])\\&\quad+\int_{\rho_{\text{ref}}}^{\rho} d\rho'\left(\frac{\partial A(\rho')}{\partial\rho'}\right)_T\\&=A_{\text{id}}[\rho,T]+\int_{\rho_{\text{ref}}}^{\rho} d\rho'\left[\left(\frac{\partial A(\rho')}{\partial\rho'}\right)_T-\left(\frac{\partial A_{\text{id}}(\rho')}{\partial\rho'}\right)_T\right].\end{aligned} \tag{5}$$

Using the substitution

$$(\partial A/\partial\rho)_T=Nk_BT/\rho+N\langle\mathcal{W}_l\rangle/\rho^2, \tag{6}$$

where $\langle\mathcal{W}_l\rangle$ is the lateral internal virial

$$\langle\mathcal{W}_l\rangle=-\frac{1}{2}\sum_{i<j}\left\langle\frac{q_{ij}^2}{r_{ij}}\frac{\partial u(r_{ij})}{\partial r_{ij}}\right\rangle, \tag{7}$$

and q_{ij} and r_{ij} are the separations of particles *i* and *j* in the *xy* plane and in three-dimensional space, respectively, we get

$$A[\rho,T]=A_{\mathrm{id}}[\rho,T]+\int_{\rho_{\mathrm{ref}}}^{\rho}d\rho'\frac{\langle\mathcal{W}_l\rangle}{\rho'}. \tag{8}$$

The free energy of a 2D ideal gas is

$$A_{\mathrm{id}}^{\mathrm{2D}}=k_BTN(\ln\rho-1)+2k_BTN\ln\Lambda, \tag{9}$$

and that of a Q2D ideal gas is

$$A_{\mathrm{id}}^{\mathrm{Q2D}}=k_BTN(\ln\rho-1)+3k_BTN\ln\Lambda -k_BTN\ln\left(\int_{-\infty}^{\infty}dz\exp[-u_{\mathrm{ext}}(z)/k_BT]\right), \tag{10}$$

where Λ is the thermal de Broglie wavelength. For the purpose of determining phase equilibrium, the last term in Eq. (9) and the last two terms in Eq. (10) can be omitted as they reappear in the expressions for the free energy density of the 2D and Q2D solids. Since a linear term in ρ in the free energy density expression does not affect the common tangent construction, we find $A_{\mathrm{id}}=A_{\mathrm{id}}^{\mathrm{2D}}=A_{\mathrm{id}}^{\mathrm{Q2D}}$ where

$$A_{\mathrm{id}}=k_BTN(\ln\rho-1). \tag{11}$$

The free energy density of the liquid then becomes

$$a^{\mathrm{liq}}[\rho,T]=k_BT\rho(\ln\rho-1)+\mathcal{A}^{-1}\int_{\rho_{\mathrm{ref}}}^{\rho}d\rho'\frac{\langle\mathcal{W}_l\rangle}{\rho'}. \tag{12}$$

As a practical procedure we fit polynomials to $\langle\mathcal{W}_l\rangle$ obtained from the simulations at different densities and then numerically integrate Eq. (12).

A different procedure was chosen for the calculation of the free energy of the solid. In this case we imagine that the interaction potential is continuously varied from that of the reference system to that of the system under investigation. Then

$$A_{\mathrm{II}}=A_{\mathrm{I}}+\int_{\mathrm{I}}^{\mathrm{II}}d\xi\left\langle\left(\frac{\partial U(\xi)}{\partial\xi}\right)\right\rangle_{\xi}, \tag{13}$$

in which the expectation value of $\partial U(\xi)/\partial\xi$ is evaluated at each point ξ along the path I→II. For the reference state we chose an Einstein crystal [15–17] with the same structure as the solid phase under consideration. This reference state is reached by slowly switching on harmonic interactions that bind the particles to their lattice sites. We execute this process via the linear bridging function

$$U(\xi)=\xi\sum_{i<j}u(r_{ij})+(1-\xi)\sum_{i}\alpha(\mathbf{q}_i-\mathbf{q}_i')^2. \tag{14}$$

In Eq. (14), $\mathbf{q}_i$ is the vector position of a particle, $\mathbf{q}_i'$ is the vector position of a lattice site in the *xy* plane, and α is twice the harmonic force constant; $\mathbf{q}$ is expressed in reduced units (relative to σ); hence α has the dimensions of energy. In the Q2D system all lattice sites are located in the plane $z=0$. The bridging function $U(\xi)$ is the same for the 2D and Q2D calculations. In the Q2D geometry, the external potential due to the plate separation is unparametrized. When $\xi=0$ the system is an Einstein crystal, $U(\xi=0)=U_E$, and when $\xi=1$ we recover the model system $U(\xi=1)=U_{\mathrm{MR}}$, where

$$U_{\mathrm{MR}}=\sum_{i<j}u(r_{ij}) \tag{15}$$

and

$$U_E=\sum_{i}\alpha(\mathbf{q}_i-\mathbf{q}_i'). \tag{16}$$

The free energy of the solid is

$$A[\rho,T]=A_E[\rho,T]+\int_0^1 d\xi\langle U_{\mathrm{MR}}-U_E\rangle_{\xi}. \tag{17}$$

Evaluation of $U(\xi)$ from Eq. (14) requires specification of α. We obtained our parametrization using a variational procedure based on the Gibbs-Bogoliubov inequality [18]

$$A\leqslant A_E(\alpha)+\langle U_{\mathrm{MR}}\rangle_{\alpha} \tag{18}$$

in which A is the free energy of the solid of interest, $A_E(\alpha)$ is the free energy of the Einstein crystal, and $\langle\cdots\rangle_{\alpha}$ denotes an ensemble average for the Einstein crystal with force constant 2α. The value of α is chosen to minimize $A_E(\alpha)+\langle U_{\mathrm{MR}}\rangle_{\alpha}$ at a given density and temperature. For a strictly two-dimensional system, $\langle U_{\mathrm{MR}}\rangle_{\alpha}$ can be computed by performing a one-dimensional integration. The probability density that in an Einstein crystal particles *i* and *j* are separated by a distance $q_{ij}\equiv|\mathbf{q}_{ij}|$ is

$$P(q_{ij})=3\alpha/k_BT\exp(-\alpha\Delta^2/2k_BT)q_{ij} \times\exp(-\alpha/2k_BTq_{ij}^2)I_0(\alpha\Delta q_{ij}/k_BT). \tag{19}$$

In Eq. (19), Δ is the lattice constant and I_0 is the zero-order modified Bessel function of the first kind. The reduced lattice constant Δ is computed for hexagonal packing (triangular lattice symmetry) and is a function of the two-dimensional density. For the strictly two-dimensional system

$$\langle U_{\mathrm{MR}}\rangle_{\alpha}=\int_0^{\infty}dq_{ij}P(q_{ij})U_{\mathrm{MR}}(q_{ij}). \tag{20}$$

In this case the value of α that minimizes $A_E(\alpha)+\langle U_{\mathrm{MR}}\rangle_{\alpha}$ is easily and quickly determined. We used the same value of α for the quasi-two-dimensional system with the same density. The free energy of a 2D Einstein crystal with given value of α is

$$A_E(\alpha)=Nk_BT\ln\left(\frac{\alpha}{\pi k_BT}\right). \tag{21}$$

We omit from Eq. (21) terms that reappear in the liquid free energy expression as they play no role in locating the transition line.

The center of mass of the simulation sample was kept fixed throughout the calculations to prevent wandering of the system in the *xy* plane as $\xi \rightarrow 1$ causing the value of $\langle U_E \rangle_\xi$ to explode. Then, the free energy of the system with fixed center of mass was corrected to account for that constraint. The free energy of a crystal with fixed center of mass is

$$A^{\text{c.m.}}(\alpha) = A_E^{\text{c.m.}}(\alpha) + \int d\xi \langle U_{\text{MR}} - U_E \rangle_\xi^{\text{c.m.}}, \tag{22}$$

where the superscript c.m. denotes a fixed center of mass. The Helmholtz free energy of an Einstein crystal with fixed center of mass is

$$A_E^{\text{c.m.}}(\alpha) = A_E(\alpha) - k_B T \ln\left(\frac{\alpha}{\pi N k_B T}\right) \tag{23}$$

with $A_E(\alpha)$ given by Eq. (23). The fixing of the center of mass of the system in the *xy* plane eliminates two degrees of freedom, so the free energies of two-dimensional and quasi-two-dimensional crystals with and without fixed centers of mass differ by $k_B T \ln \mathcal{A}$. The free energy density for the crystal phase, $a = A/\mathcal{A}$, is

$$a(\rho,T) = \rho k_B T \ln\left(\frac{\alpha}{\pi k_B T}\right) + \rho \int_0^1 d\xi (\langle u_{\text{MR}} \rangle_\xi - \alpha \langle q^2 \rangle_\xi) + \frac{k_B T}{\mathcal{A}} \ln\left(\frac{\pi \rho k_B T}{\alpha}\right). \tag{24}$$

In Eq. (24) $\langle q^2 \rangle$ is the mean square displacement in the *xy* plane and $u_{\text{MR}} = N^{-1} U_{\text{MR}}$. The integral appearing in Eq. (24) was evaluated via a polynomial fit to ten values of the integrand. For the strictly two-dimensional system all points at $\xi = 0$ were obtained from a one-dimensional integration using Eq. (19).

Although it is convenient to choose the hard-disk system as reference when the thermodynamics of a dense strictly two-dimensional system is studied, both because there are very accurate data available for its free energy as a function of density [19] and because the thermodynamic properties of the hard-disk liquid can be obtained with good precision from one or the other of several accurate analytical forms for the equation of state [20], we have chosen differently. It is because we are concerned with the contribution of the out-of-plane motion to the thermodynamic properties of a quasi-two-dimensional system that we have adopted the procedure described above. Then, so as to be able to consistently compare the properties of the quasi-two-dimensional and the strictly two-dimensional systems, we used the same procedure to calculate the free energy as a function of density and temperature for both systems.

C. Calculation of elastic constants

The KTHNY theory [5,6] of 2D melting predicts that a continuous solid-to-hexatic transition occurs when

$$K = \left(\frac{8}{\sqrt{3}}\right) \frac{1}{\rho k_B T} \left(\frac{\mu(\mu+\lambda)}{2\mu+\lambda}\right) = 16\pi, \tag{25}$$

where μ and λ are the Lamé elastic constants of our model solid. When $K = 16\pi$ the solid becomes unstable with respect to the proliferation of dislocations, quasi-long-range order is destroyed and the system loses its resistance to shear stress. However, a first-order melting transition may intercede before a 2D solid reaches the point of dislocation binding instability. It has been suggested by Chui [9] that melting of a 2D solid occurs when grain boundary (i.e., line defect) proliferation occurs; he showed that grain boundary proliferation will occur before dislocation binding instability if the core energy of a dislocation, E_c, is less than $2.84 k_B T$.

So as to better compare the results of our simulations with the predictions of the KTHNY theory of two-dimensional melting, we have calculated the Lamé elastic constants μ and λ of our model solid. We describe first the calculation of the bare elastic constants.

The shear modulus μ was calculated from the measured stress as a function of applied strain [21,22]. A uniform shear strain was imposed on the simulation sample by modifying the boundary conditions via the following coordinate transformation:

$$x' = x + \varepsilon_{xy} y,$$

$$y' = y. \tag{26}$$

The stress τ_{xy} that is associated with the strain ε_{xy} is calculated from the ensemble average

$$\tau_{xy} = \frac{1}{\mathcal{A}} \sum_{i<j} \left\langle \frac{x_{ij} y_{ij}}{r_{ij}} \frac{\partial u(r_{ij})}{\partial r_{ij}} \right\rangle_{\varepsilon_{xy}}, \tag{27}$$

where $\mathcal{A}'$ is the deformed area of the periodic simulation box and, as usual, $r_{ij} = |\mathbf{r}_i - \mathbf{r}_j|$, $x_{ij} = x_i - x_j$, and $y_{ij} = y_i - y_j$. When only a pure shear strain is applied to the simulation cell $\mathcal{A}' = \mathcal{A}$. To ensure that the applied shear strain produced only a linear response in the simulation sample, and no plastic flow, we restricted the shear strain applied to the simulation sample to be less than 2% and calculated the shear modulus at a specified density for two or more distinct values of the strain applied:

$$\mu = \frac{\tau_{xy}(\varepsilon_{xy})}{\varepsilon_{xy}} + O(\varepsilon_{xy}). \tag{28}$$

The second Lamé constant λ is related to the shear modulus and the bulk modulus by

$$\lambda = \rho \left(\frac{\partial p_l}{\partial \rho}\right) - \mu, \tag{29}$$

which is valid for a two-dimensional system. We calculate the bulk modulus by fitting a convenient polynomial to the lateral pressure versus density data obtained from the simulations, and then taking the derivative of that function. The lateral pressure p_l was calculated from the lateral internal virial $\mathcal{W}_l$ [Eq. (7)]

$$p_l = N k_B T \rho + \mathcal{A}^{-1} \langle \mathcal{W}_l \rangle. \tag{30}$$

All of the elastic constant values reported in this paper are from simulations performed on a perfect defect-free crystal. Bates and Frenkel [22] have shown that two-dimensional hard-disk systems with and without vacancies have nearly identical bare elastic constants.

As already noted, a key prediction of the KTHNY theory is that continuous melting of a two-dimensional solid to a hexatic phase will occur when Eq. (25) is satisfied. Because of fluctuations in the 2D and Q2D systems, the bare elastic constants described above are renormalized by long-wavelength phonons and by the presence of defects. Bates and Frenkel [22] have shown that the contribution to the renormalization of the elastic constants by long-wavelength phonons is very weak. They have also shown that although lattice defects have little influence on the bare elastic constants in the hard-disk system (and the same is true for the systems we have studied) they make a large contribution to the renormalization of the elastic constants, and are responsible for a gross reduction of their values. The renormalization of the elastic constants by dislocations can be estimated using the KTHNY theory recursion relations [4–6]

$$\frac{\partial K^{-1}}{\partial l} = 3\pi y^2 \exp\left(\frac{K}{8\pi}\right)\left[\frac{1}{2} I_0\left(\frac{K}{8\pi}\right) - \frac{1}{4} I_1\left(\frac{K}{8\pi}\right)\right],$$

$$\frac{\partial y}{\partial l} = \left(2 - \frac{K}{8\pi}\right) y + 2\pi y^2 \exp\left(\frac{K}{16\pi}\right) I_0\left(\frac{K}{8\pi}\right), \tag{31}$$

where l is related to the linear dimension of the simulation sample as $l = \ln(r/\Delta)$, $y = \exp(-E_c/k_B T)$ is the fugacity of the dislocation pairs, E_c is the core energy of a dislocation, and I_0 and I_1 are modified Bessel functions. The bare values of the elastic constants were used as initial data for the KTHNY recursion relation. The core energy was obtained from the probability density (per unit area) of formation of a dislocation pair [8,23], namely,

$$p_d = \exp(-2E_c/k_B T) Z(K),$$

$$Z(K) = \frac{16\sqrt{3}\pi^2}{K - 8\pi} I_0\left(\frac{K}{8\pi}\right) \exp\left(\frac{K}{8\pi}\right). \tag{32}$$

Values of p_d were determined by direct count from the simulation data.

III. PHASE EQUILIBRIA IN Q2D AND 2D COLLOID ASSEMBLIES

It is relevant to recall the results of the simulation studies of the model colloid assembly with the MR potential reported by Zangi and Rice [14]. Those calculations were restricted to the isotherm $T^* = 1.00$. They found that at this temperature and for densities up to $\rho^* = 0.90$ the system supports first-order liquid-to-hexatic and hexatic-to-solid transitions. At higher densities the system supports an isostructural solid I–solid II transition and a buckling transition, both of which are continuous. The dislocation pair, free dislocation, and free disclination concentrations deviated seriously from those expected from the KTHNY theory. The results of our simulations fill in the phase diagram for $T^* < 1.00$. It is found that the critical temperature for the solid I–solid II transition is about $T^* \approx 0.6$. The liquid–solid I–solid II triple point temperature is about $T^* \approx 0.45$. For $T^* < 0.6$ both the quasi-two-dimensional and the strictly two-dimensional colloid assemblies support a liquid phase, and three solid phases with hexagonal packing but different nearest neighbor separations. All of these phase transitions have first-order character. For $T^* > 0.6$ the structure of the phase diagram is like that found by Zangi and Rice.

In the text to follow we discuss the distribution of nearest neighbor separations, $P(r_{12})$, and its relationship with the MR potential. The distribution of nearest neighbors is defined by

$$P(r_{12}) = \frac{1}{N} \sum_{i=1}^{N} \frac{1}{n_i} \sum_{j=1}^{n_i} \langle \delta(r_{12} - r_{ij}) \rangle, \tag{33}$$

where the sum over j is over the n_i nearest neighbors of particle i, r_{ij} is the distance between particles i and j in the xy plane, and the distribution along z is

$$P(z) = \frac{1}{N} \sum_{i=1}^{N} \langle \delta(z - z_i) \rangle, \tag{34}$$

where z_i is the location of particle i along z.

As noted in the last section, we have computed the phase boundaries for the 2D and Q2D model systems by the common tangent procedure. Prior to calculating the common tangents, polynomial expressions were fitted to the Helmholtz free energy density, a, as a function of density for each phase, and the pressure and chemical potential of a phase were calculated as functions of density. Figure 1 displays a superposition of the phase boundaries in the 2D and Q2D colloid assemblies we have studied. The phase boundaries near the liquid–solid I–solid II triple point and near the critical point of the isostructural solid I–solid II transition are not shown because they could not be accurately calculated (due to fluctuations in the system). The change in the phase boundaries when a 2D system becomes a Q2D system is a signature of the influence of out-of-plane motion on the thermodynamic properties of the system (the particles are the same).

As already mentioned, both the 2D and Q2D systems with the MR potential support an isostructural solid I–solid II transition; the two solid phases have different nearest neighbor separation distributions. In both the 2D and Q2D systems the higher density solid phase (II) close to the solid I–solid II phase boundary has a unimodal distribution of nearest neighbor separations with a narrow peak centered at $r^* = 1.05$ (Fig. 2), which is the location of the attractive well in the MR interaction. The distribution of nearest neighbor separations in the lower density solid phase, in both 2D and Q2D systems, has two separated peaks connected by an approxi-

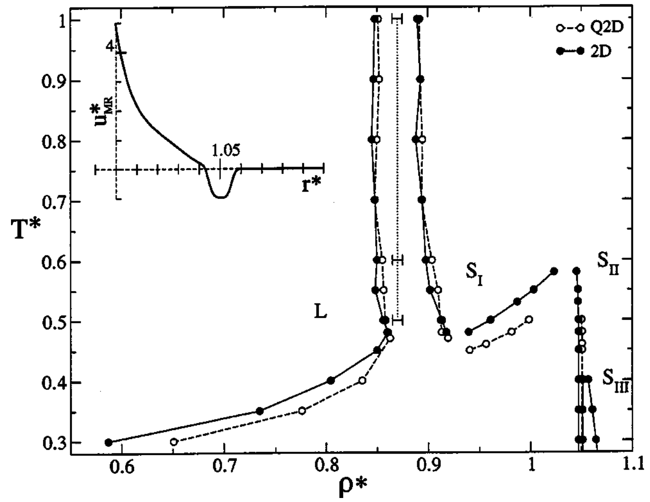

FIG. 1. Phase boundaries for the 2D and Q2D systems. L, S_{I}, S_{II}, and S_{III} denote the stable liquid, solid I, solid II, and solid III, respectively. The solid III phase of the Q2D system is not indicated. The dotted line connects the density points for $T^*=1.00$, 0.60, and 0.50 where the square-root Lorentzian becomes a better fit than the Lorentzian for the q-dependent structure function, thereby indicating the liquid-hexatic transition (Sec. V). For both the 2D and Q2D systems at all temperatures the density at which it occurs is $\rho^*=0.87\pm0.005$. The inset contains the Marcus-Rice pair potential $u^*_{\mathrm{MR}}(r^*)$, where r^* is the interparticle distance.

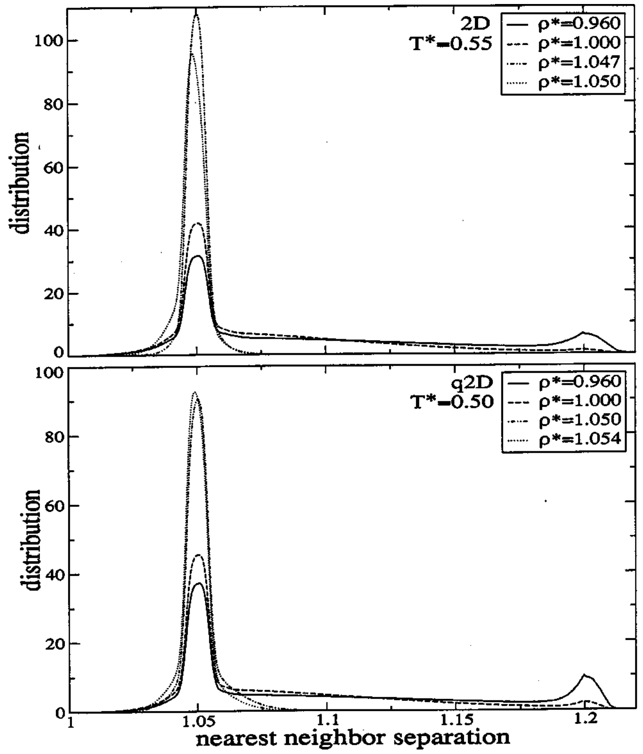

FIG. 2. Nearest neighbor separation distribution functions for the 2D and Q2D models for different densities at $T^*=0.55$ and 0.50, respectively. At these temperatures the density ranges of the solid I–solid II coexistence regions are (1.00–1.047) and (1.00–1.050) for the 2D and Q2D systems, respectively.

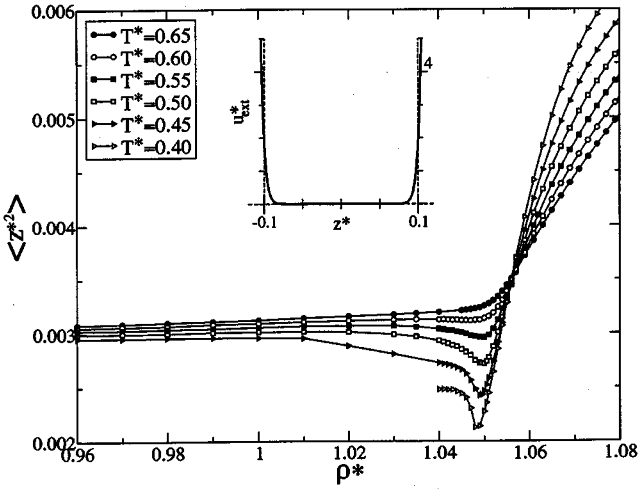

FIG. 3. Mean square amplitude of out-of-plane displacement as a function of density in the Q2D system. $T^*=0.65$ is above the solid I–solid II critical temperature, $T^*=0.60,0.50,0.45$ spans the range between the critical and the triple point temperatures, and $T^*=0.40$ is below the triple point temperature. The inset contains the colloid-wall potential $u^*_{\mathrm{ext}}(z^*)$, where z^* is the distance from the center of the cell to the colloid particle.

mately linear curve. The larger of the two peaks corresponds to the position of the attractive well in the MR interaction and the smaller peak is centered at $r^*\approx1.2$ which is larger than the lattice constant. The twofold discrete character of the nearest neighbor separation distribution indicates increased density fluctuation due to the close vicinity of the critical point. As the density of a solid I approaches the solid I–solid II phase boundary the larger peak grows and the smaller peak becomes smaller until it almost completely disappears and only the approximately linear connecting component remains. Of course, in the 2D system there is no out-of-plane motion. In the Q2D system the mean square amplitude of the out-of-plane motion in solid I is much larger than that of the same motion in solid II. The data displayed in Fig. 3 show that in the solid I–solid II coexistence region the mean square amplitude of out-of-plane displacement $\langle z^{*2}\rangle$ is nearly density independent at all temperatures for $\rho^*<1.04$, and that there is a small increase in the mean square amplitude of out-of-plane displacement with increasing temperature. However, close to the solid I–solid II phase boundary, centered around $\rho^*=1.05$, there is a drastic decrease in the mean square amplitude of out-of-plane displacement. In the vicinity of this density point the lattice constant approaches a length that corresponds to the location of the attractive well in the MR potential. As density continues to increase particles begin to separate into two layers to accommodate the increase in packing without losing the energetic advantage of placement in the attractive well of the MR potential. This separation is increasingly emphasized with decreasing temperature. Figure 4 displays the distributions of colloid particles along z for several densities at fixed temperature and several temperatures at fixed density. At any given temperature above the critical point the distribution along z separates into two layers with increasing density as

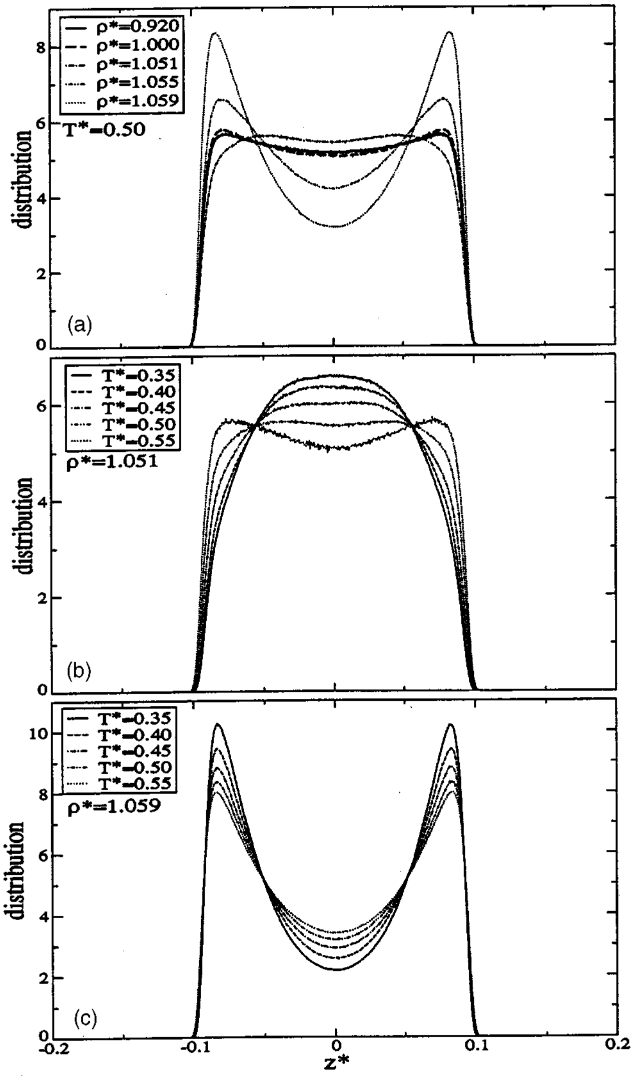

FIG. 4. Distribution of colloid particles along the z axis (a) at $T^*=0.50$ for various densities; bold and regular lines correspond to the solid I and solid II phase, respectively; (b) for solid II at $\rho^*=1.051$ for various temperatures; and (c) for solid II at $\rho^*=1.059$ for various temperatures.

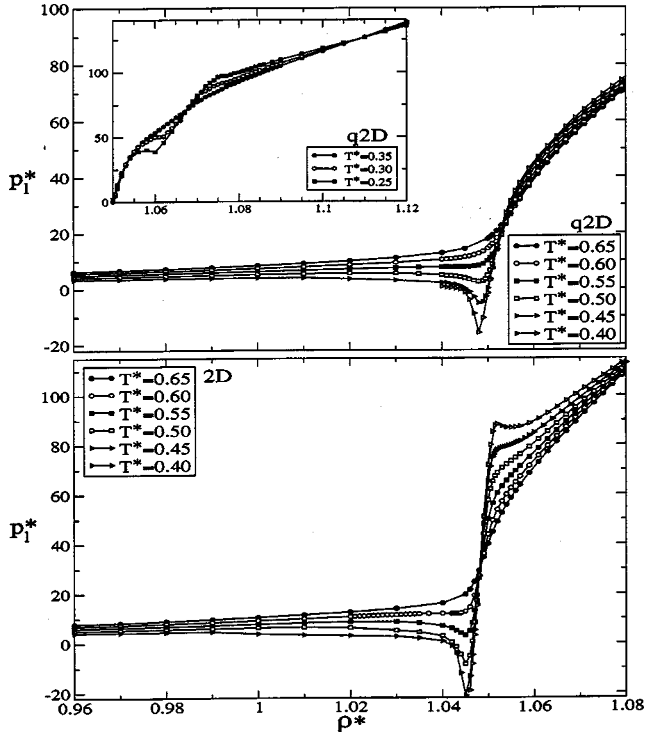

FIG. 5. Lateral pressure p_l^* versus ρ^* for different temperatures for the 2D and Q2D systems.

each particle becomes increasingly more confined to one side of the cell. Below the critical point the same behavior is observed separately for the solid I phase and the solid II phase but when solid I changes into solid II particles are forced into the center [Fig. 4(a)]. As temperature decreases, and the entropic demands of the system diminish, the distribution along z becomes even more centralized, so a greater fraction of particles can occupy the attractive well of the MR potential [Fig. 4(b)]. The temperature dependent behavior of the distribution along z is reversed at only slightly higher density; particles become increasingly more confined to one side of the cell [Fig. 4(c)].

In the solid I–solid II coexistence region in both the 2D and Q2D systems the longitudinal (in the plane) pressure p_l [Eq. (30)] drops dramatically (Fig. 5). As expected, as the density is increased further there is a rapid rise in the longitudinal pressure in the Q2D system, but the derivative $(\partial p_l/\partial \rho)_T$ is much smaller for the Q2D system than for the 2D system. The rapid rise in p_l signals the separation at which there is onset of the repulsive component of the MR potential. In the Q2D case the stress induced by the repulsive part of the MR potential is relieved via the system's separation into two layers.

We note that the high density side of the solid I–solid II coexistence line is nearly vertical. For the strictly 2D system the density along this part of the coexistence line is $\rho^*=1.0470\pm0.0005$. For the Q2D system the density along this part of the coexistence line is slightly higher, $\rho^*=1.0505\pm0.0005$.

It is clear that converting a 2D system to a Q2D system by permitting out-of-plane motion leads to a shift of some of the phase boundaries to higher density. These shifts are most visible for the low density portion of the phase boundaries where solid II is involved. The coexistence region not involving solid II, the liquid–solid I coexistence, is very nearly the same for the 2D and Q2D systems. The introduction of the out-of-plane motion increases the entropy of the phase but the gain in entropy is uneven among different phases. The mean square amplitude of the out-of-plane displacement is nearly density independent across the liquid–solid I coexistence as is the distribution along z. However, when the liquid or solid I crosses to the solid II phase the mean square amplitude of the out-of-plane displacement decreases (Fig. 3) and the distribution along z (Fig. 4) is forced into a monolayer around $z=0$ so as to reduce interparticle distance, allowing more particles to occupy the attractive well of the MR potential; the entropy contribution to the free energy is sacrificed to gain the enthalpy contribution.

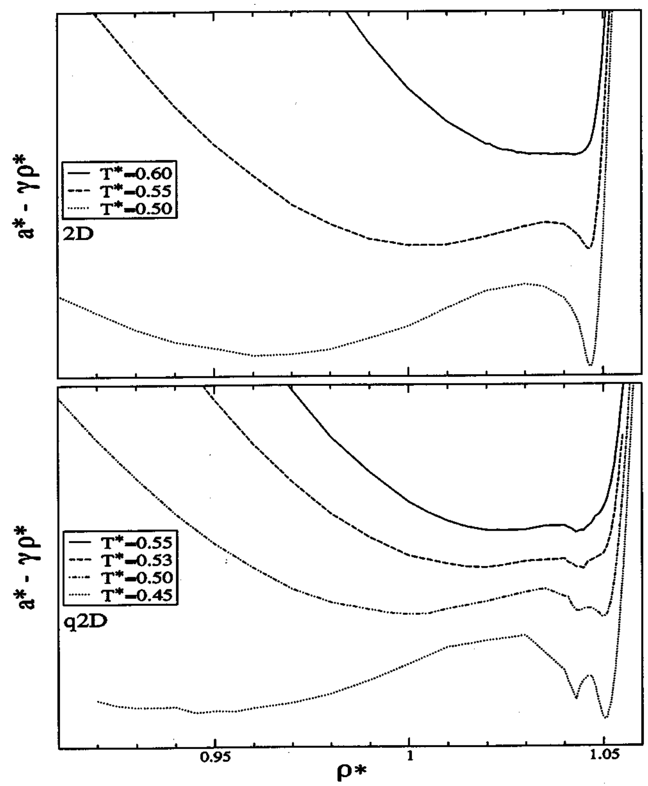

FIG. 6. Free energy density a^* minus the linear fit $\gamma\rho^*$ vs ρ for different temperatures for the 2D and Q2D systems displaying the solid I-solid II coexistence region.

Further information concerning differences between the phase diagrams of the 2D and Q2D model colloid systems can be obtained from analysis of the free energy density versus density curves. Figure 6 displays, for the solid I–solid II coexistence region, $a^*(\rho^*)-\gamma\rho^*$ versus ρ^*, where γ is an arbitrary constant; the subtraction of $\gamma\rho^*$ from $a^*(\rho^*)$ does not change the common tangent construction. In the strictly 2D system there are either one ($T^*>0.60$) or two ($T^*<0.60$) minima of $a^*(\rho^*)$ in the density range displayed. The density region between two minima corresponds to phase coexistence. At the critical temperature the two free energy minima merge into one. Clearly the critical point for the solid I–solid II transition is close to $T^*=0.6$ in this system. In the Q2D system there are one ($T^*>0.60$), two ($0.60>T^*>0.53$), or three ($T^*<0.53$) minima of $a^*(\rho^*)$ in the density range displayed. For three minima two possible tangent constructions can be effected but only one corresponds to stable phases.

Both the 2D and Q2D systems support solid II–solid III isostructural transitions at high density. This phase transition can be inferred, for the 2D system, by examining the lateral pressure in Fig. 5 and the phase boundaries of this transition are indicated in Fig. 1 at densities higher than that of pure solid II; the critical temperature for this transition is about $T^*\approx 0.45$. Statistical fluctuations of the free energy prevented us from computing the phase boundaries for the Q2D system by the common tangent construction. Nevertheless, the van der Waals loop of the lateral pressure at $T^*=0.25$ for the Q2D system (inset to Fig. 5) indicates the presence of a transition. To understand the nature of the solid II–solid III transition we concentrate on results for the 2D system for which the transition point can be identified with precision. The distribution of nearest neighbor separations in the 2D system at the solid II–solid III transition is unimodal for solid II and bimodal for solid III with the much larger peak corresponding to the minimum and the smaller peak to the soft repulsive component of the MR potential (Fig. 7). As the density of solid III increases, the distribution eventually becomes unimodal with all interparticle separations corresponding to the position of the soft repulsive component of the MR potential. This indicates that solid II–solid III transition is induced by the soft repulsive component of the MR potential; particles begin to climb the repulsive potential at high density when the lattice constant is less than the minimum in the MR potential.

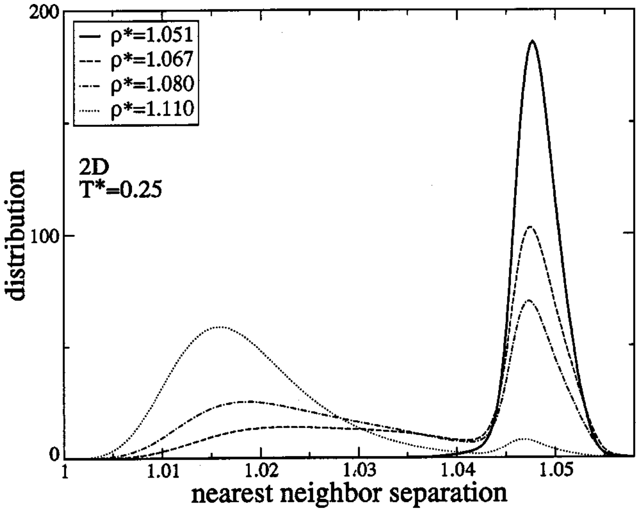

FIG. 7. Nearest neighbor separation distribution functions for the 2D system at $T^*=0.25$ for various densities across the solid II–solid III coexistence region ($1.051<\rho^*<1.061$). Bold line corresponds to the nearest neighbor separation distribution function of solid II.

Another consequence of the repulsive component of the pair potential at high density for both the 2D and Q2D systems is the condition $(\partial p_l/\partial T)_\rho<0$ as seen in Fig. 5. $(\partial p_l/\partial T)_\rho<0$ is equivalent to $(\partial s/\partial\rho)_T>0$, where s is the entropy per particle. By climbing the repulsive potential particles gain spatial freedom and the system's entropy increases. This condition appears to hold for all temperatures studied in this paper and spans the density range from the close packed density to $\rho^*\approx 1.1$. When the temperature is low enough, the soft repulsion component of the interaction is significant enough to induce a first-order phase transition to the solid III phase.

In the Q2D system the solid II–solid III transition is shifted to higher density and lower temperature as a result of out-of-plane motion. Before particles start climbing the barrier of the pair potential, they separate into two layers along z at both sides of the cell thereby extending the density range in which particles can occupy the minimum of the pair potential, hence shifting the solid II–solid III transition to higher density. The lateral pressure of the Q2D system in Fig. 5 (inset) displays two plateaus. The low density plateau corresponds to the separation of the solid II phase into layers

TABLE I. Lateral pressure p_l^*, shear modulus μ^*, bulk modulus $B^*=\rho^*\partial p_{l,\mathrm{fit}}^*/\partial\rho^*$, and elastic constant $K/16\pi$ as a function of the density for 2D at $T^*=1.00$.

ρ^*	p_l^*	$B^*=\rho^*\left(\frac{\partial p^*_{l,\mathrm{fit}}}{\partial\rho^*}\right)$	μ^*	$K/16\pi$
0.890	8.705±0.002	40.4±0.4	18.6±0.2	1.32±0.04
0.900	9.159±0.002	44.3±0.4	22.0±0.1	1.50±0.03
0.910	9.671±0.002	49.1±0.4	25.8±0.1	1.70±0.03
0.920	10.241±0.002	54.9±0.4	30.4±0.1	1.96±0.03
0.930	10.876±0.002	62.0±0.4	35.5±0.1	2.23±0.03
0.940	11.589±0.002	70.7±0.4	42.2±0.1	2.58±0.04
0.950	12.394±0.002	81.2±0.4	50.6±0.1	3.01±0.04
0.960	13.301±0.002	94.3±0.4	60.5±0.2	3.53±0.04
0.970	14.363±0.002	110.3±0.4	73.7±0.2	4.18±0.04
0.980	15.585±0.002	130.4±0.4	90.1±0.3	5.02±0.04
0.990	17.024±0.003	156.2±0.4	111.9±0.4	6.05±0.05
1.000	18.764±0.003	191.2±0.4	143.5±0.4	7.53±0.05
1.010	20.915±0.003	243.1±0.4	188.1±0.4	9.65±0.05
1.020	23.712±0.003	329.7±0.4	258.9±0.4	13.06±0.06
1.030	27.615±0.004	493.6±0.4	373.6±0.4	18.97±0.06
1.040	33.786±0.005		567.3±0.4	
1.050	45.298±0.005		864.5±0.8	
1.060	64.341±0.006		1048.7±0.8	

TABLE II. Lateral pressure p_l^*, shear modulus μ^*, bulk modulus $B^*=\rho^*\partial p_{l,\mathrm{fit}}^*/\partial\rho^*$, and elastic constant $K/16\pi$ as a function of the density for 2D at $T^*=0.60$.

ρ^*	p_l^*	$B^*=\rho^*\left(\frac{\partial p^*_{l,\mathrm{fit}}}{\partial\rho^*}\right)$	μ^*	$K/16\pi$
0.900	4.998±0.002	20.1±0.7	11.6±0.2	1.2±0.1
0.910	5.245±0.002	22.8±0.4	13.9±0.2	1.45±0.07
0.920	5.509±0.002	25.9±0.4	16.3±0.1	1.67±0.06
0.930	5.826±0.002	29.4±0.4	19.6±0.1	1.93±0.06
0.940	6.149±0.002	33.2±0.4	23.5±0.1	2.24±0.06
0.950	6.524±0.002	37.6±0.4	28.3±0.1	2.60±0.06
0.960	6.934±0.002	42.5±0.4	34.2±0.1	3.02±0.06
0.970	7.414±0.002	48.0±0.4	42.5±0.1	3.56±0.06
0.980	7.910±0.003	54.1±0.4	53.2±0.1	4.19±0.06
0.990	8.502±0.003	64.7±0.4	68.8±0.2	5.00±0.07
1.000	9.191±0.003	68.7±0.4	89.6±0.3	5.95±0.08
1.010	9.886±0.003	77.2±0.4	124.6±0.4	7.23±0.09
1.020	10.699±0.004	86.7±0.4	186.7±0.4	8.89±0.09
1.030	11.598±0.005	97.3±0.4	315±1	11.1±0.1
1.040	12.222±0.008		784±1	
1.050	43.474±0.007		3702±3	
1.060	73.461±0.006		1340±1	

and the high density plateau corresponds to climbing the soft repulsion of the pair potential.

IV. ELASTIC CONSTANTS: A TEST OF THE KTHNY PREDICTIONS

Because of the prominent role in the KTHNY theory of 2D melting that is played by renormalization of the system elastic constants, we have calculated the bare and renormalized Lamé constants for the 2D and Q2D model systems described in this paper. Our calculations of the bare elastic constants were based on simulation runs with the same number of particles as lattice sites. In such a system the number of vacancies must equal the number of interstitials at all times. The simulation was always started from the perfect, defect-free, crystal obtained by straining the triangular lattice by ε_{xy}. We have verified, from model simulations with artificially large numbers of vacancies, that for our systems the calculated bare elastic constants are insensitive to the presence of vacancies. The results of our calculations are displayed in Table I, II, and III for the 2D system, for temperatures $T^*=1.00$, 0.60, and 0.50, respectively, and in Tables IV, V, and VI for the Q2D system for temperatures $T^*=1.00$, 0.60, and 0.50, respectively. The uncertainties in the lateral pressure p_l and shear modulus B quoted in these tables are the statistical errors associated with finite time collection of values of fluctuating quantities. The uncertainty quoted for the bulk modulus was estimated by changing the form of the polynomial fit to pressure. Note that we were unable to calculate elastic constants very close to the transition densities (located by the condition of equal pressure and chemical potential) of either system, although we could get closer for the 2D than for the Q2D system. In neither system do the calculated values of $K/16\pi$ derived from the bare elastic constants fall below unity before the transition density is reached.

We now consider the calculated values of the renormalized elastic constants. Figure 8 shows E_c as a function of the density for the 2D and Q2D systems. For both systems, near the transition density $E_c^*/T^*\approx 6$, a value safely larger than the limit $E_c^*/T^*=2.84$ below which grain boundary proliferation is predicted to generate a first-order melting transition. To obtain the dislocation unbinding melting density we fitted our calculated values of K and E_c as a functions of density to convenient polynomials; these polynomial fits were used as input data for the KTHNY recursion relations [Eq. (31)]. The KTHNY recursion equations were then solved numerically via Euler discretization to obtain the renormalized value of $K=K_R$. Figure 9 displays the density dependencies of K_R for the 2D and Q2D systems. In each

TABLE III. Lateral pressure p_l^*, shear modulus μ^*, bulk modulus $B^*=\rho^*\partial p_{l,\mathrm{fit}}^*/\partial\rho^*$, and elastic constant $K/16\pi$ as a function of the density for 2D at $T^*=0.50$.

ρ^*	p_l^*	$B^*=\rho^*\left(\frac{\partial p^*_{l,\mathrm{fit}}}{\partial\rho^*}\right)$	μ^*	$K/16\pi$
0.910	4.029±0.002	15.8±0.2	9.6±0.3	1.20±0.07
0.920	4.196±0.002	17.5±0.2	12.0±0.1	1.42±0.05
0.930	4.407±0.002	19.3±0.2	14.5±0.1	1.64±0.05
0.940	4.621±0.002	21.3±0.2	17.2±0.2	1.86±0.05
0.950	4.851±0.002	23.5±0.2	21.0±0.2	2.15±0.05
0.960	5.129±0.002	25.9±0.2	25.8±0.2	2.47±0.05

TABLE IV. Lateral pressure p_l^*, shear modulus μ^*, bulk modulus $B^*=\rho^*\partial p_{l,\mathrm{fit}}^*/\partial\rho^*$, and elastic constant $K/16\pi$ as a function of the density for Q2D at $T^*=1.00$.

ρ^*	p_l^*	$B^*=\rho^*\left(\frac{\partial p_{l,\mathrm{fit}}^*}{\partial\rho^*}\right)$	μ^*	$K/16\pi$
0.900	7.460±0.003	35.0±0.2	16.7±0.1	1.39±0.02
0.910	7.862±0.003	38.7±0.2	19.9±0.1	1.59±0.02
0.920	8.308±0.003	43.2±0.2	23.1±0.1	1.80±0.02
0.930	8.810±0.003	48.6±0.2	27.3±0.1	2.07±0.03
0.940	9.365±0.003	55.2±0.2	31.8±0.1	2.36±0.03
0.950	9.987±0.004	63.1±0.2	38.0±0.1	2.75±0.03
0.960	10.696±0.004	72.6±0.2	45.2±0.1	3.20±0.03
0.970	11.507±0.004	84.1±0.2	54.6±0.1	3.76±0.03
0.980	12.427±0.004	97.9±0.2	66.6±0.1	4.46±0.03
0.990	13.515±0.004	117.5±0.2	82.6±0.1	5.40±0.03
1.000	14.818±0.004	142.1±0.2	103.9±0.2	6.62±0.03
1.010	16.387±0.005	175.9±0.2	132.1±0.3	8.24±0.04
1.020	18.354±0.005	227.6±0.2	174.8±0.3	10.67±0.05
1.030	20.967±0.005	316.9±0.2	240.9±0.4	14.65±0.05
1.040	24.764±0.005		345.9±0.7	
1.050	30.870±0.005		516.0±0.7	
1.060	41.429±0.005		719.2±0.8	

part of the figure the vertical lines mark the density at which we located a transition by use of the thermodynamic condition of equality of pressure and chemical potential. Starting with the 2D system, and moving from high to low density, we find that when $T^*=0.60$ the KTHNY theory barely preempts the first-order melting transition from solid to hexatic, and when $T^*=1.00$ and 0.50 the ordinary thermodynamic first-order transition from the solid to the hexatic phase preempts the KTHNY transition between those phases. Our result for $T^*=0.60$ is sensibly the same as found by Sengupta, Nielaba, and Binder [23] and by Watanabe *et al.* [24] for the 2D assembly of hard disks. On the other hand, for the Q2D system, again moving from high to low density, we find that when $T^*=1.00$ and 0.50 the ordinary thermodynamic first-order transition from the solid to the hexatic phase preempts the KTHNY transition between those phases.

It is also interesting to examine the elastic constants at

TABLE V. Lateral pressure p_l^*, shear modulus μ^*, bulk modulus $B^*=\rho^*\partial p_{l,\mathrm{fit}}^*/\partial\rho^*$, and elastic constant $K/16\pi$ as a function of the density for Q2D at $T^*=0.60$.

ρ^*	p_l^*	$B^*=\rho^*\left(\frac{\partial p_{l,\mathrm{fit}}^*}{\partial\rho^*}\right)$	μ^*	$K/16\pi$
0.900	4.104±0.002	16.9±0.2		
0.910	4.283±0.002	18.7±0.2	10.6±0.1	1.37±0.04
0.920	4.511±0.002	20.7±0.2	12.6±0.1	1.56±0.04
0.930	4.744±0.002	23.0±0.2	15.0±0.1	1.80±0.04
0.940	5.006±0.002	25.8±0.2	17.8±0.1	2.06±0.04
0.950	5.299±0.002	29.0±0.2	21.1±0.1	2.36±0.04
0.960	5.615±0.003	32.8±0.2	24.9±0.2	2.71±0.05
0.970	5.976±0.003	37.3±0.2	31.4±0.1	3.23±0.04
0.980	6.399±0.003	42.6±0.2	39.0±0.1	3.82±0.04
0.990	6.844±0.003	48.9±0.2	48.6±0.2	4.52±0.06
1.000	7.384±0.003	56.3±0.2	63.2±0.3	5.47±0.06
1.010	7.967±0.003	65.0±0.2	85.9±0.3	6.73±0.07
1.020	8.674±0.004	75.2±0.2	120.3±0.7	8.34±0.1
1.030	9.456±0.004	87.3±0.2	189.2±0.7	10.66±0.1
1.040	10.517±0.005		347±2	
1.050	14.608±0.007		1126±3	
1.060	39.673±0.009		1412±3	

TABLE VI. Lateral pressure p_l^*, shear modulus μ^*, bulk modulus $B^*=\rho^*\partial p_{l,\mathrm{fit}}^*/\partial\rho^*$, and elastic constant $K/16\pi$ as a function of the density for Q2D at $T^*=0.50$.

ρ^*	p_l^*	$B^*=\rho^*\left(\frac{\partial p_{l,\mathrm{fit}}^*}{\partial\rho^*}\right)$	μ^*	$K/16\pi$
0.920	3.440±0.002	14.1±0.2	9.2±0.2	1.38±0.07
0.930	3.595±0.002	15.6±0.2	11.2±0.1	1.54±0.05
0.940	3.781±0.002	17.1±0.2	13.2±0.1	1.75±0.05
0.950	3.960±0.002	18.8±0.2	16.0±0.1	2.01±0.04
0.960	4.171±0.002	20.7±0.2	19.4±0.1	2.30±0.05
0.970	4.399±0.002	22.7±0.2	23.4±0.1	2.62±0.06
0.980	4.647±0.002	24.9±0.2	29.1±0.2	3.01±0.06
0.990	4.917±0.002	27.2±0.2	36.5±0.2	3.47±0.06
1.000	5.180±0.002	29.8±0.2	48.0±0.2	4.05±0.06

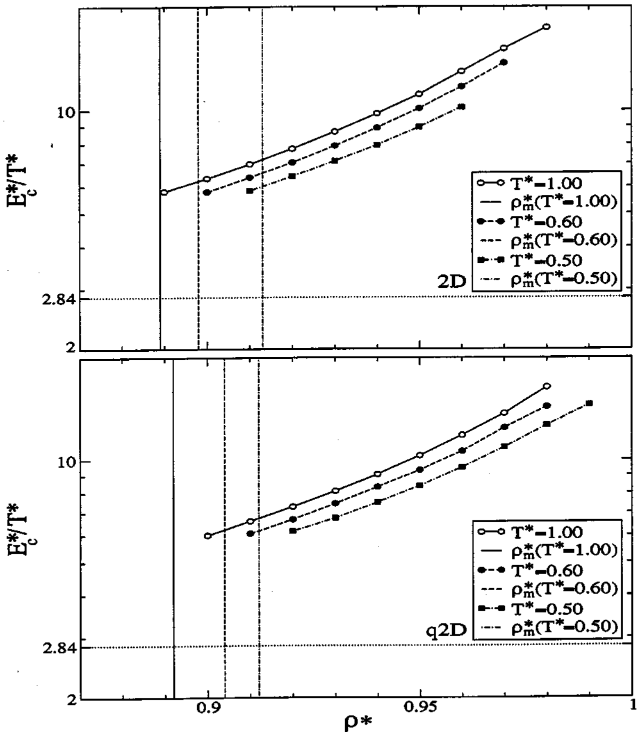

FIG. 8. Core energy E_c^*/T^* for the 2D and Q2D systems at $T^*=1.00$, 0.60, and 0.50 as a function of density. Note that $E_c^*/T^*>2.84$. The vertical lines mark the first-order melting density.

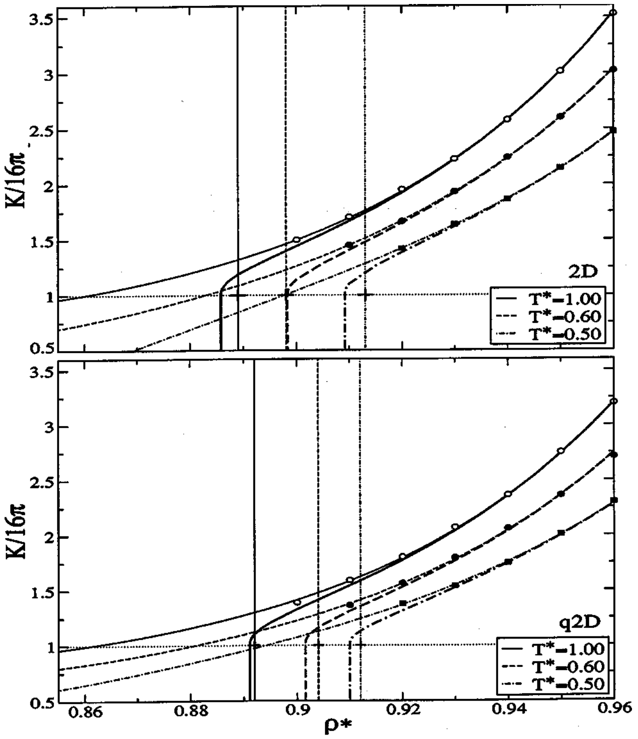

FIG. 9. Renormalization of $K/16\pi$ (bold lines) obtained from the recursion relation for the 2D and Q2D systems at $T^*=1.00$, 0.60, and 0.50 as a function of density. Symbols indicate calculated $K/16\pi$ data points. Regular width lines are obtained from fitting data points. The vertical lines mark the first-order melting densities.

temperatures below the estimated triple point temperature $T_3^*\approx 0.45$. The coexistence region for $T^*<T_3^*$ differs from that for $T^*>T_3^*$ in that the particle configurations clearly indicate the presence of two distinct phases. When $\rho^*=1.051$, slightly above the melting density $\rho_m(T^*)=1.0505$, we find that $K/16\pi=755\pm 3$. Moreover, as the melting density is approached from above $K/16\pi$ increases (at $\rho^*=1.055$, $K/16\pi=381\pm 4$ and at $\rho^*=1.060$, $K/16\pi=183\pm 3$) which is the opposite behavior to that observed for temperatures above T_3^*.

For both the 2D and Q2D systems at $T^*=0.60$ and 0.50 there is a density region of the solid I phase where $B<\mu$ (Tables II, III, V, and VI). The condition $B<\mu$ generates a negative value for Poisson's ratio $\sigma_P=(B-\mu)/(B+\mu)$. A solid that is characterized by $\sigma_P<0$ will, if stretched along one direction, expand in the transverse direction.

At the critical point $B=0$ and in a finite region surrounding the critical point B is small enough that the combination of elastic constants that defines $K/16\pi$ is less than 1. Outside this region, and close to the melting line, our calculations never yield a value of $K/16\pi$ that is less than 1. The $T^*=0.60$ isotherm of the 2D system displays a van der Waals loop that is indicative of a first-order solid I–solid II transition. The $T^*=0.62$ isotherm of the 2D system no longer displays a van der Waals loop, and at the density that this isotherm is "flattest," $\rho^*=1.035$, we find $B^*=166\pm 2$, $\mu^*=456\pm 2$, and $K/16\pi=19.6\pm 0.4$. The $T^*=0.54$ isotherm of the Q2D system displays a van der Waals loop, whereas the $T^*=0.55$ isotherm does not. At the density that this isotherm is "flattest," $\rho^*=1.040$, we find $B^*=19.0\pm 0.2$, $\mu^*=322\pm 2$, and $K/16\pi=3.6\pm 0.1$. It seems that the system we have studied supports only a very small region with $K/16\pi<1$, and the resolution in density of our simulations fails to capture its presence.

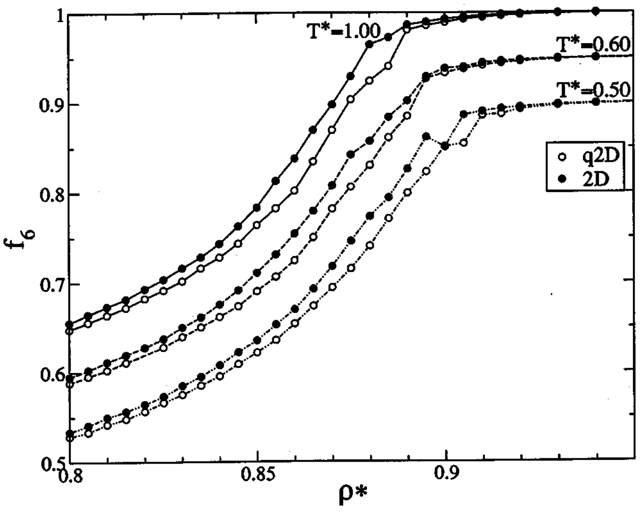

FIG. 10. Fractions of six-coordinated particles f_6 as a function of density for the 2D and Q2D systems at $T^*=1.00$, 0.60, and 0.50; $f_6(T^*=0.60)$ and $f_6(T^*=0.50)$ are shifted by $\Delta f_6=0.05$ and $\Delta f_6=0.1$, respectively, to capture the influence of the out-of-plane motion for each temperature.

V. IDENTIFYING THE HEXATIC PHASE

Arguably the most interesting feature of packing in a dense 2D system is the existence of a hexatic phase. We examined our simulation data with an eye toward identifying when a phase found in the 2D and Q2D systems we studied has hexatic structure. To make this identification we examined the bond orientation order, the structure function, and the q-dependent shape of the diffraction peak for both 2D and Q2D systems.

We start our analysis with examination of the defect structure revealed by the Voronoi mapping of the real space configuration of the particles in the 2D and Q2D systems. This mapping generates a space covering set of polygons. A perfect hexagonal crystal has a Voronoi map with only six-sided figures. Polygons in the Voronoi map that have fewer or more than six sides are identified as defects. A decrease in temperature shifts $f_6(\rho^*)$ to greater ρ^* while keeping the shape of the curve the same. One consequence of this shift is an increase in melting density with decreasing temperature. Figure 10 compares f_6 in the 2D and Q2D systems as a function of density at several temperatures. Juxtaposition of the $f_6(\rho^*)$ curves of the 2D and Q2D systems shows that allowing out-of-plane motion (when 2D⇒Q2D) produces a shift similar to that produced when the temperature is decreased in either of the model systems.

The local orientational order parameter for particle i is defined by [5,6]

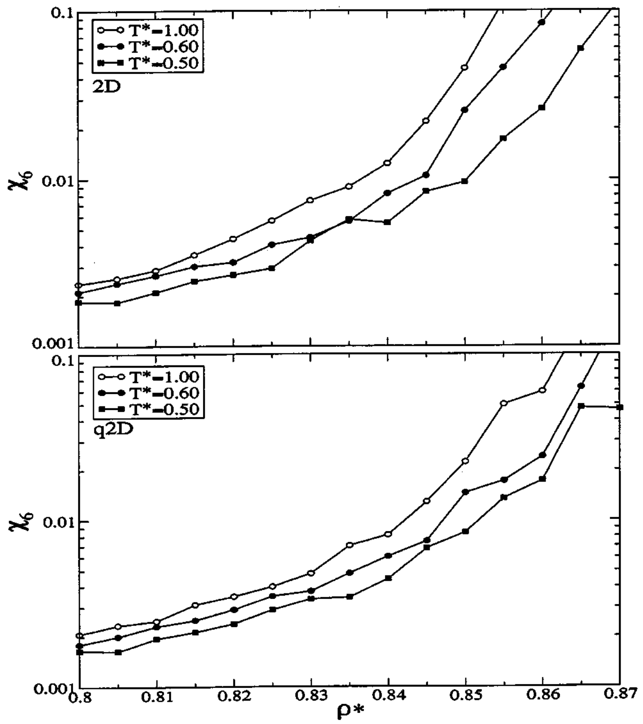

FIG. 11. Bond orientation parameter susceptibility χ_6^* as a function of density for the 2D and Q2D systems.

$$\psi_{6,i} \equiv \frac{1}{n_i} \sum_{j=1}^{n_i} \exp(6 i \theta_{ij}), \tag{35}$$

where the sum over j is over the n_i nearest neighbors of particle i, and θ_{ij} is the angle formed by the line (bond) between particles i and j and an arbitrary but fixed reference direction. The global bond orientation order parameter is defined by

$$\Psi_6 = \left| \frac{1}{N} \sum_{i=1}^{N} \psi_{6,i} \right|. \tag{36}$$

The susceptibility of the bond orientation parameter χ_6, which measures the size of the fluctuations in Ψ_6, is

$$\chi_6 = N(\langle \Psi_6^2 \rangle - \langle \Psi_6 \rangle^2). \tag{37}$$

For densities less than the transition density $\rho_{l \to h}$, KTHNY theory predicts that the bond orientation correlation function decays as $\exp(-r/\xi_6)$ with a correlation length that diverges as $\rho \to \rho_{l \to h}$ from lower density:

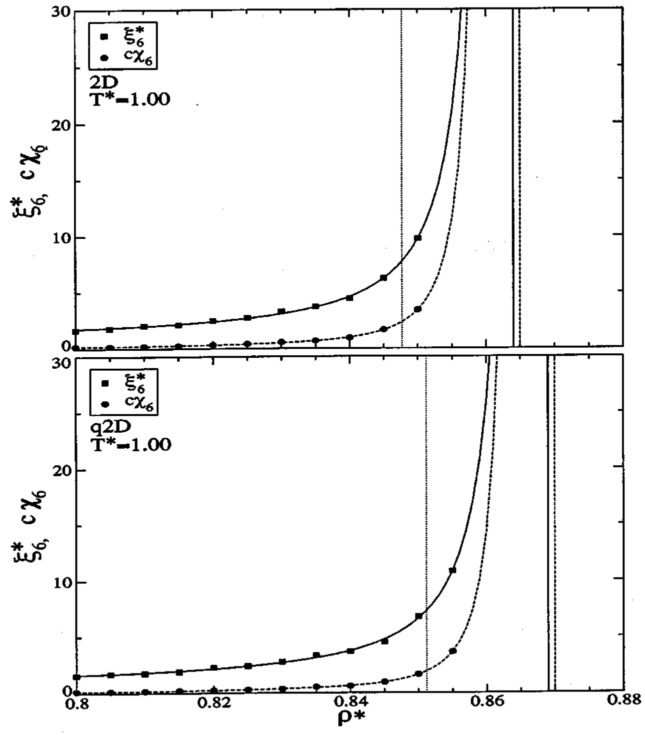

FIG. 12. ξ_6^* and $c\chi_6$, c being an arbitrary constant, together with the best fits for KTHNY behavior as a function of density for the 2D and Q2D systems. The critical values of ρ^* are visualized by vertical lines. Dotted vertical line is the freezing density from free energy calculation. We used points in the ranges $0.800 \leqslant \rho^* \leqslant 0.850$ and $0.800 \leqslant \rho^* \leqslant 0.855$ for the 2D and Q2D systems, respectively, to make the fit.

$$\xi_6(t) = a_\xi \exp(b_\xi t^{-1/2}). \tag{38}$$

The bond orientation parameter susceptibility also diverges as

$$\chi_6(t) = a_\chi \exp(b_\chi t^{-1/2}), \tag{39}$$

where $t \equiv \rho_{l \to h} - \rho$. In the hexatic phase the bond orientation correlation function decays as $r^{-\eta_6(\rho)}$; when $\rho = \rho_{l \to h}$ the value of the exponent is $\eta_6 = 1/4$. In the thermodynamic limit, both the liquid phase and the hexatic phase have $\langle \Psi_6 \rangle = 0$; hence χ_6 is nearly equal to $\langle \Psi_6^2 \rangle$. At the melting density $\langle \Psi_6 \rangle$ assumes a finite value and increases toward unity as the density increases. Near the freezing transition, as ξ_6 becomes comparable with a linear dimension of the simulation box, the model system becomes susceptible to an un-

TABLE VII. ρ_i^* obtained from best fit for the critical behavior of the correlation length ξ_6^* and susceptibility χ_6.

System	T	Fit	Range	ρ_i^*	Range	ρ_i^*	$\max(\xi_6/\sqrt{A})$
2D	1.00	ξ_6	0.800–0.850	0.864	0.820–0.850	0.862	0.22
		χ_6	0.800–0.850	0.865	0.820–0.850	0.864	0.22
Q2D	1.00	ξ_6	0.800–0.855	0.869	0.820–0.855	0.868	0.22
		χ_6	0.800–0.855	0.870	0.820–0.855	0.870	0.22

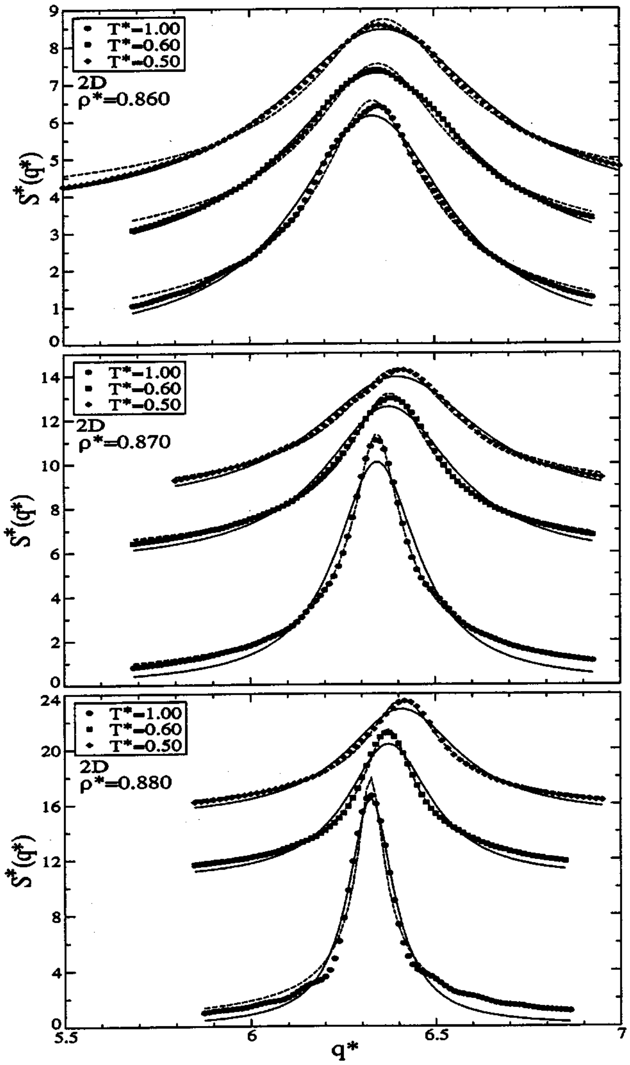

FIG. 13. q^*-dependent structure function $S^*(q^*)$ for densities spanning the coexistence region, $\rho^*=0.860$, 0.870, and 0.880, for $T^*=1.00$, 0.60, and 0.50 for the 2D system. $S^*(q^*)$ curves were shifted to be fitted on one graph.

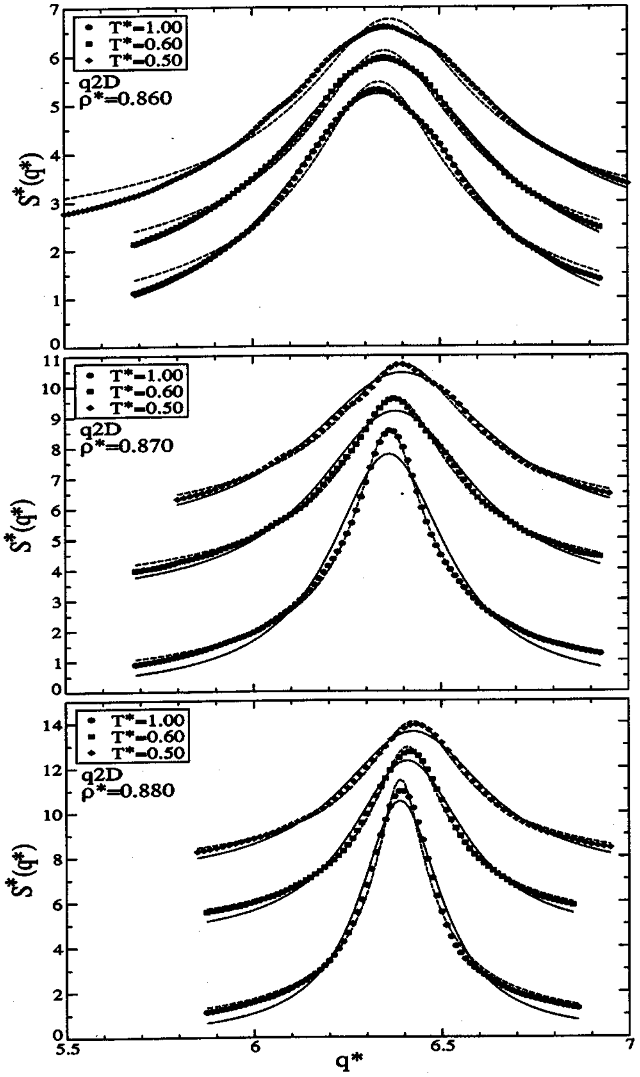

FIG. 14. q^*-dependent structure function $S^*(q^*)$ for densities spanning the coexistence region, $\rho^*=0.860$, 0.870, and 0.880, for $T^*=1.00$, 0.60, and 0.50 for the Q2D system. $S^*(q^*)$ curves were shifted to be fitted on one graph.

physical transition. Discrimination between a real and an unphysical transition requires a careful analysis of the size dependence of the behavior of the system studied.

We now evaluate the parameters that appear in the KTHNY mechanical instability description of the melting transition and attempt to capture the temperature dependent behavior of the "would-be" transition density for comparison with the temperature dependent freezing densities evaluated from the thermodynamic criterion of phase equilibrium, namely, equality of the pressure and chemical potentials of the two phases. To accomplish this task we use the bond susceptibility χ_6 and the correlation length ξ_6 as monitors of the transition. Moreover, we use only data for densities where finite-size effects are minimal, that is, where the correlation length is significantly smaller than the box edge length. These data were fitted to Eqs. (38) and (39) to locate the transition density. The correlation length was obtained from fitting the bond orientation correlation function with an ansatz of the form [25]

$$g_6(r)=ar^{-\eta_6}\exp(-r/\xi_6), \tag{40}$$

where r is the actual particle-particle separation. The susceptibility was calculated from its thermodynamic limit $\chi_6=\langle\Psi_6^2\rangle$.

Figure 11 displays χ_6 as a function of density at various temperatures for the 2D and Q2D systems. As T^* decreases the divergence of χ_6 is displaced to higher density, thereby causing the density of the transition to increase. Note that at any given temperature the passage from a 2D to a Q2D system produces a similar effect, namely, the high density limit of the stability of the more disordered phase is increased. This behavior is in agreement with the results of our free energy calculations for these systems.

The ξ_6 and χ_6 data were fitted to the analytic forms displayed in Eqs. (38) and (39), respectively, where η_6 was set to 1/4. In each case the last data point used corresponds to the last state point for which the instantaneous value of Ψ_6

fluctuates around a single value (at the next data point Ψ_6 fluctuates about two distinct values). We found that the ratio $\xi_6/\sqrt{\mathcal{A}}$ for the last usable data point is about 0.2. We note that Jaster [25] employed a tighter bound, namely, $\xi_6/\sqrt{\mathcal{A}} < 0.06$, to select simulation data that are free of finite-size effects.

The results of the fits of ξ_6 and χ_6 for the 2D and Q2D systems with $T^* = 1.00$ are collected in Table VII. The transition densities obtained from ξ_6 are systematically lower than those obtained from χ_6 by 0.001. A fitting that omits some data points that are furthest from the transition density shifts the predicted 2D transition density to slightly smaller values, but has no effect on the predicted Q2D transition densities. The values of ξ_6 and χ_6 obtained in the fashion described, and the fitted curves, are displayed in Fig. 12. These figures show that the transition density predicted by the KTHNY criterion falls in the coexistence region predicted from the free energy calculations; the overestimate of the transition density is about $\delta\rho^* = 0.02$.

We now examine the shapes of the peaks in the structure function. In a conventional 2D or 3D liquid the q dependence of $S(q)$ near the peaks is well approximated by the Lorentzian function

$$S(q) \propto \frac{1}{(q-q_0)^2 + (1/\xi)}. \tag{41}$$

In contrast, close to the hexatic-liquid transition, in the hexatic phase, the q dependence of $S(q)$ near the peaks is predicted to have the form [26]

$$S(q) \propto \left[\frac{1}{(q-q_0)^2 + (1/\xi)}\right]^{1/2}, \tag{42}$$

where ξ is the positional correlation length and q_0 is the maximum of a peak. The structure function was calculated by explicit evaluation of the expression

$$S(\mathbf{q}) = N^{-1}\left\langle \left(\sum_{i=1}^{N} \cos(\mathbf{q}\cdot\mathbf{r}_i)\right)^2 + \left(\sum_{i=1}^{N} \sin(\mathbf{q}\cdot\mathbf{r}_i)\right)^2 \right\rangle, \tag{43}$$

where $\mathbf{r}$ is measured in the xy plane. In the hexatic phase $S(\mathbf{q})$ has sixfold modulation as a function of the angle θ_q between a reference axis and the vector $\mathbf{q}$. The relevant function for our purpose is the average of $S(\mathbf{q})$ over the angular range $0 < \theta_q < \pi/3$:

$$S(q) = \frac{3}{\pi}\int_0^{\pi/3} d\theta_q S(\mathbf{q}). \tag{44}$$

The results of this calculation of $S(q)$ and the fits of the peaks to Eqs. (41) and (42) are shown for different temperatures and densities in Fig. 13 for the 2D system and in Fig. 14 for the Q2D system. The solid and dashed lines are, respectively, fits to the Lorentzian and square-root-Lorentzian line shapes. For the same thermodynamic state the first peak in the structure function of the Q2D system is broader than the corresponding peak in the structure function of the 2D system. Regardless of temperature and dimensionality, the density at which the square-root-Lorentzian function provides a better fit to the peak shape is $\rho^* \approx 0.87$. Analysis of the free energies of the liquid and solid phases yields a first-order transition with liquid density that varies only slightly with temperature and dimensionality and is $\rho^* \approx 0.85$ as long as $T^* \geqslant 0.50$. To better visualize the location of the liquid-to-hexatic transition determined from the fit to a q-dependent structure function in relation to the liquid–solid I coexistence region predicted from the free energy calculations we connect the density points $\rho^* = 0.87$ at $T^* = 1.00$, 0.60, and 0.50 on the phase diagram graph (Fig. 1).

ACKNOWLEDGMENTS

This work was supported by the National Science Foundation under Grant No. NSF CHE-9977841. We have also benefited from support from the National Science Foundation funded MRSEC Laboratory at the University of Chicago.

---

[1] N. D. Mermin, Phys. Rev. **176**, 250 (1968).

[2] R. Peierls, *Suprises in Theoretical Physics* (Princeton University Press, Princeton, NJ, 1979).

[3] J. M. Kosterlitz and D. J. Thouless, J. Phys. C **5**, L124 (1972).

[4] J. M. Kosterlitz and D. J. Thouless, J. Phys. C **6**, 1181 (1973).

[5] B. I. Halperin and D. R. Nelson, Phys. Rev. Lett. **41**, 121 (1978).

[6] D. R. Nelson and B. I. Halperin, Phys. Rev. B **19**, 2457 (1979).

[7] A. P. Young, Phys. Rev. B **19**, 1855 (1979).

[8] D. S. Fisher, B. I. Halperin, and R. Morf, Phys. Rev. B **20**, 4692 (1979).

[9] S. T. Chui, Phys. Rev. B **28**, 178 (1983).

[10] P. Bladon and D. Frenkel, Phys. Rev. Lett. **74**, 2519 (1995).

[11] G. M. Kepler and S. Fraden, Phys. Rev. Lett. **73**, 356 (1994).

[12] A. H. Marcus and S. A. Rice, Phys. Rev. E **55**, 637 (1997).

[13] T. Chou and D. R. Nelson, Phys. Rev. E **53**, 2560 (1996).

[14] R. Zangi and S. A. Rice, Phys. Rev. E **58**, 7529 (1998).

[15] J. Q. Broughton and G. H. Gilmer, J. Chem. Phys. **79**, 5095 (1983).

[16] D. Frenkel and A. J. C. Ladd, J. Chem. Phys. **81**, 3188 (1984).

[17] D. Frenkel and B. Smit, *Understanding Molecular Simulation: From Algorithms to Applications* (Academic, San Diego, CA, 1996).

[18] J. P. Hansen and D. McDonald, *Theory of Simple Liquids* (Academic Press, New York, 1986).

[19] B. J. Alder, W. G. Hoover, and D. Y. Young, J. Chem. Phys. **49**, 3688 (1968).

[20] A. Santos, M. López de Haro, and S. B. Yuste, J. Chem. Phys. **103**, 4622 (1995).

[21] J. Q. Broughton, G. H. Gilmer, and J. D. Weeks, Phys. Rev. B **25**, 4651 (1982).
[22] M. A. Bates and D. Frenkel, Phys. Rev. E **61**, 5223 (2000).
[23] S. Sengupta, P. Nielaba, and K. Binder, Phys. Rev. E **61**, 6294 (2000).
[24] H. Watanabe, S. Yukawa, Y. Ozeki, and N. Ito, Phys. Rev. E **66**, 041110 (2002).
[25] A. Jaster, Physica A **264**, 134 (1999); Phys. Rev. E **59**, 2594 (1999).
[26] G. Aepple and R. Bruinsma, Phys. Rev. Lett. **53**, 2133 (1984).